

Available online at www.sciencedirect.com

SciVerse ScienceDirect

journal homepage: www.elsevier.com/locate/ije

A direct ethanol anode for solid oxide fuel cell based on a chromite-manganite with catalytic ruthenium nanoparticles

N.K. Monteiro^a, F.B. Noronha^b, L.O.O. da Costa^b, M. Linardi^a, F.C. Fonseca^{a,*}

^a Instituto de Pesquisas Energéticas e Nucleares, IPEN-CNEN/SP, São Paulo, SP 05508-000, Brazil

^b Instituto Nacional de Tecnologia – INT, Av. Venezuela 82, 20081-312 Rio de Janeiro, Brazil

ARTICLE INFO

Article history:

Received 6 February 2012

Received in revised form

26 March 2012

Accepted 29 March 2012

Available online 25 April 2012

Keywords:

Solid oxide fuel cells

Chromite-manganite anode

LSCM

Direct ethanol

Internal reforming

Hydrogen production

ABSTRACT

La_{0.75}Sr_{0.25}Cr_{0.50}Mn_{0.50}O₃ (LSCM) perovskite was studied aiming at effective anodes for direct (dry) ethanol fueled solid oxide fuel cells. Both the transport and catalytic properties of LSCM were studied in compounds with partial substitutions of either Mn or Cr by Ru (LSCM-Ru). X-ray diffraction data evidenced that single phase compounds were obtained at 1200 °C, without significant structural distortions upon Ru addition. Under reducing atmosphere both the exsolution of Ru nanoparticles to the surface of LSCM grains and enhanced electronic conductivity of LSCM-Ru samples were observed. Solid oxide single fuel cells tests showed that LSCM-Ru anodes have higher performance running on direct ethanol than on hydrogen. Such an increase in fuel cell performance was correlated to both the enhanced electronic transport and the catalytic properties of LSCM-Ru. The catalytic tests revealed that Ru addition enhanced the stability of LSCM and suppressed carbon deposition under ethanol, indicating that such compound is a promising anode for direct ethanol solid oxide fuel cell.

Copyright © 2012, Hydrogen Energy Publications, LLC. Published by Elsevier Ltd. All rights reserved.

1. Introduction

A major goal of the research on solid oxide fuel cells (SOFCs) is the development of components for stable operation using fuels containing carbon. The efficient use of fuels other than hydrogen is considered as an important step for bridging the gap toward commercialization of SOFCs. However, the cermet Ni/yttria-stabilized zirconia (Ni/YSZ), the most common anode material of SOFCs, exhibits low tolerance to redox cycles and high tendency for carbon deposition [1–6]. Such serious limitations have encouraged the development of alternative anode materials to replace Ni-based cermets. In this context, oxides with perovskite structure ABO₃ doped with transition metals are interesting candidates for such application. These ceramic anodes have low activity for

carbon formation and allow the control of their physico-chemical properties by chemical substitutions at both sites A and B of the crystal structure [1].

Among proposed materials to replace the Ni/YSZ cermet, the chromite-manganite La_{0.75}Sr_{0.25}Cr_{0.5}Mn_{0.5}O₃ (LSCM) has attracted a great deal of interest [1,7,8]. This ceramic anode is stable under redox cycles and has good electrochemical activity for hydrogen [1,2,9]. However, because the p-type conductivity this compound exhibits a considerable drop of the electrical conductivity in low oxygen partial pressures, and has limited catalytic activity as compared to the Ni-cermet [1–4]. Different strategies have been used to overcome such restrictions, mainly using the LSCM in conjunction with other materials, either metallic nanoparticles or ceramic phases such as Pd and doped-ceria, respectively [10–12]. In

* Corresponding author. Instituto de Pesquisas Energéticas e Nucleares, IPEN-CNEN/SP, Av. Prof. Lineu Prestes 2242, 05508-000 Sao Paulo, SP, Brazil. Tel./fax: +55 11 31339282.

E-mail address: fcfonseca@ipen.br (F.C. Fonseca).

0360-3199/\$ – see front matter Copyright © 2012, Hydrogen Energy Publications, LLC. Published by Elsevier Ltd. All rights reserved.
doi:10.1016/j.ijhydene.2012.03.157

general, such studies have investigated the addition of impregnated phases aiming at enhanced electrical conductivity and/or catalytic activity for different fuels, including methane, propane, and ethanol [8,13].

For ethanol fueled SOFCs, LSCM/YSZ [14] composites were studied for the direct oxidation of the alcohol and LSCM [15], LSCM/ceria, and LSCM/scandia-stabilized zirconia (ScSZ) [16] composites were investigated for ethanol/water mixtures. The studies using LSCM-based composites for ethanol fueled SOFC reported no apparent carbon formation, whilst for LSCM anode a small amount of carbon deposition was observed; nonetheless, the single cells were stable during the short term operation [14–16]. In addition, it was reported that the performance of the LSCM-based anode was significantly improved by the addition of impregnated metallic nanoparticles of Pd [14] and Cu [16]. Such an improvement of the electrochemical properties of the LSCM electrodes has been usually achieved by the dispersion of fine metallic particles through impregnation of a metallic salt in the porous (pre-sintered) electrode structure. However, when such a method is used for SOFCs electrodes, it can result in compositional inhomogeneities and particle coarsening due to the high temperatures used for fabrication and operation of the fuel cell [17]. Therefore, instead of impregnating metallic nanoparticles in SOFC anodes, an alternative route in which the metallic phase initially forms a solid solution and upon a heat treatment segregates as nanoparticles has been used. Upon heat treatment in reducing atmosphere, the metal, usually Ni or Ru, partially exudes from the perovskite crystal structure and precipitates as nanoparticles (or nanoclusters) [17–20] onto the surface of the parent compound. Such segregation of the metal usually takes place during the initial hours of operation of the SOFC and was observed to result in particles/clusters with rather stable size (few nanometers), high dispersion, and low coarsening rate over the period of the operation of the SOFC [20]. Such features contributed to high catalytic activity for fuel oxidation, carbon deposition suppression, and resulted in a significant decrease of the anode polarization resistance [7,8,18].

In this present study, the synthesis and detailed characterization of $\text{La}_{0.75}\text{Sr}_{0.25}\text{Cr}_{0.5}\text{Mn}_{0.5}\text{O}_3$ (LSCM) with partial substitution of either Cr or Mn for ruthenium Ru (LSCM-Ru) are presented. The main goal is the development of a ceramic material for hydrogen production, with enhanced transport properties and catalytic activity, to be used as the anode in direct ethanol SOFCs.

2. Experimental

A polymeric precursor method was used for the synthesis of ceramic anodes $\text{La}_{0.75}\text{Sr}_{0.25}\text{Cr}_{0.50-x}\text{Mn}_{0.50-y}\text{Ru}_{x,y}\text{O}_3$, where $x, y = 0, 0.05, 0.10$, and 0.20 [21]. In this paper, the compounds are represented by LSC(x%)M(y%)-Ru; for example, $x = 0.20$ is referred as LSC20M-Ru, and $y = 0.05$ as LSCM5-Ru.

The starting metallic salts were lanthanum nitrate hexahydrate (99.99%), strontium nitrate (>99%), manganese acetate tetrahydrate (>99%), chromium nitrate nonohydrate (>99%), and ruthenium III chloride hydrate (99.98%); all from Sigma–Aldrich. The amounts of citric acid (CA) and ethylene

glycol (EG) followed the ratio 60:40 (CA: EG) by weight, and the molar ratio between CA and metal ions was 3:1. Initially, citric acid, ruthenium chloride and distilled water were mixed at $\sim 70^\circ\text{C}$ under magnetic stirring. After ~ 15 min, the remaining cations were added to the solution, followed by the addition of EG. The resulting solution was kept under magnetic stirring and evaporated at constant temperature $\sim 70^\circ\text{C}$ to obtain the precursor resin. The polymeric resin was pre-calcined at 300°C for 1 h, followed by homogenization in agate mortar and calcination at 800°C for 5 h. The obtained powders were treated in air in the temperature range of 1000 – 1400°C . Cylindrical pellets were formed by uniaxial pressing of calcined (800°C) powders and sintering at 1400°C for 1 h in air. Some experiments were performed with samples reduced by heat treatment under hydrogen flow (25 mL min^{-1}) at 800°C for 4 h.

Phase characterization was carried out by X-ray diffraction (XRD) in the 2θ range of 20° – 90° , with step of 0.05° (2θ) and counting time of 2 s, using Cu $K\alpha$ radiation in a Rigaku Desktop Miniflex diffractometer. The morphology of LSCM-Ru powders was analyzed by scanning electron microscopy (SEM) in a FEI Quanta 600 FEG and by transmission electron microscopy (TEM) in a JEOL JEM 2100.

Temperature programmed reduction (TPR) experiments were carried out on a Micromeritics TPD/TPR 2900 apparatus. The sample (30 mg) was pre-treated at 500°C for 1 h under air flow (50 mL min^{-1}) prior to the TPR experiment in order to remove traces of water. Reduction profiles were then recorded by passing a stream of $10\% \text{H}_2/\text{Ar}$ at a flow rate of 50 mL min^{-1} , while the sample was heated at a rate of $10^\circ\text{C min}^{-1}$ from ambient temperature to 900°C . A cold-trap was placed just before the thermal conductivity detector (TCD) of the instrument to remove the water from the exit stream.

Electrical resistance measurements were performed by 4-probe using a Lakeshore 370 resistance bridge. A digital multimeter (Keithley 2000) monitored the temperature measured by a type K thermocouple positioned close to the sample. Bar samples, cut from cylindrical pellets, with Ag contact pads cured at 600°C , were measured in both static air and a mixture containing $4\% \text{H}_2$ balanced with Ar, from room temperature up to 800°C during heating and cooling (3°C min^{-1}).

Single cells were fabricated using $8\text{ mol}\%$ yttria-stabilized zirconia (YSZ, Tosoh, Japan) cylindrical substrates, sintered at 1600°C , with 18 mm diameter and 0.5 mm thickness. $\text{La}_{0.65}\text{Sr}_{0.3}\text{MnO}_3$ (LSM) cathodes and LSCM-Ru anodes were deposited by spin-coating, using suspensions based on terpeneol and ethyl cellulose. After the deposition of each electrode, a heat treatment at 800°C for organics removal was followed by sintering at 1400°C and 1150°C for the anode and cathode, respectively. Anode performance was also investigated with an interfacial layer of Ni/YSZ ($40/60\text{ vol}\%$), with $\sim 10\text{ }\mu\text{m}$ thickness, deposited following the same procedure. Au and Pt mesh current collectors were attached, using the correspondent metal ink, to the surfaces of the anode and cathode, respectively, and cured at 800°C . Single cells with active electrode area of 0.78 cm^2 were sealed on the extremity of an alumina tube sample holder, with the anode side facing the inner part of the tube, by using Aremco 552 cement. The sample holder (alumina tube and single cell) is inserted in a resistive horizontal tube furnace and connected to the

metallic heads of a homemade test station with 4 Pt wires for electrical contacts and alumina capillary tubes for gas delivery. Single cell tests using hydrogen (3 vol.% H₂O) were carried out at fixed temperatures during heating in the 800–950 °C range. At 950 °C, hydrogen was switched to ethanol. Ethanol was gasified by bubbling N₂ through anhydrous ethanol at a fixed temperature. In our experiments, N₂ was bubbled through anhydrous ethanol at 50 °C, which resulted in a gas composition of ~30% ethanol determined from the saturation vapor pressure for ethanol at 1 atm. The electrochemical data were collected during cooling down in the 950 °C–800 °C temperature range. During the tests, synthetic air was delivered to the cathode. Gas flow rates were set to 50 mL min⁻¹ by mass flow controllers and the temperature was monitored by a thermocouple placed close to the cathode side. Polarization curves and open circuit impedance spectroscopy measurements were performed using a Zahner IM6 potentiostat.

Direct ethanol decomposition (ED), steam reforming (SR), and partial oxidation (POX) of ethanol were performed in a fixed-bed reactor at atmospheric pressure. Prior to reaction, catalysts were reduced under pure hydrogen (30 mL min⁻¹) at 800 °C for 1 h and then purged under N₂ at the same temperature for 30 min. All reactions were carried out at 800 °C. Partial oxidation (POX) was conducted using an O₂/ethanol molar ratio of 0.5. For SR, H₂O/ethanol molar ratio of 3.0 was used. The reactant mixtures were obtained using two saturators containing water and ethanol, which were maintained at the temperature required to obtain the desired H₂O/ethanol and O₂/ethanol molar ratios. For ED and POX, N₂ (30 mL min⁻¹) and 5.6% O₂/N₂ mixture (30 mL min⁻¹), respectively, were flown through the saturator with ethanol, and then the reactant mixtures obtained were diluted with N₂ (N₂ stream flowed at 30 mL min⁻¹). In the case of SR, the reactant mixture was obtained by flowing two N₂ streams (30 mL min⁻¹) through each saturator containing ethanol and water separately. The partial pressure of ethanol was maintained constant for all experiments. The variation of partial pressure of water was compensated by a decrease in the partial pressure of N₂.

In order to observe the catalyst deactivation within a short timeframe, a small amount of catalyst was used (20 mg). The samples were diluted with inert SiC (SiC mass/catalyst mass = 3.0). The reaction products were analyzed by gas chromatography (Micro GC Agilent 3000 A) containing two channels for dual thermal conductivity detectors (TCD) and two columns: a molecular sieve and a Poraplot U column. The ethanol conversion and selectivity to products were determined from:

$$X_{\text{ethanol}} = \frac{(n_{\text{ethanol}})_{\text{fed}} - (n_{\text{ethanol}})_{\text{exit}}}{(n_{\text{ethanol}})_{\text{fed}}} \times 100 \quad (1)$$

$$S_x = \frac{(n_x)_{\text{produced}}}{(n_{\text{total}})_{\text{produced}}} \times 100 \quad (2)$$

where $(n_x)_{\text{produced}}$ = moles of X produced (X = hydrogen, CO, CO₂, methane, acetaldehyde or ethylene) and $(n_{\text{total}})_{\text{produced}}$ = moles of H₂ + moles of CO + moles of CO₂ + moles of methane + moles of acetaldehyde + moles of ethylene (i.e., the moles of water produced are not included).

After reactions, spent catalysts were analyzed both by SEM, using a FEI Inspect S scanning electron microscope equipped with a secondary electron analyzer, and by simultaneous thermogravimetric and differential thermal analyses (Setaran Labsys) up to 1200 °C under air flow (50 mL min⁻¹).

3. Results and discussion

3.1. Synthesis and characterization of LSCM-Ru

The phase formation of LSCM-Ru compounds was investigated by XRD analysis of samples treated in air at different temperatures. Fig. 1 shows the evolution of XRD patterns of precursor resins of LSCM, LSC20M-Ru, and LSCM20-Ru treated under air in the 600–1400 °C temperature range. The XRD patterns showed that all the samples heated at 800 °C exhibited the diffraction peaks corresponding to the LSCM phase, in accordance with thermal analysis results [22]. The LSCM-Ru compounds have perovskite structure with hexagonal symmetry, in agreement with previous studies [7,23]. However, additional peaks in the 2θ region between ~24° and 30° (dotted rectangle in Fig. 1), probably associated with SrCrO₄, indicated that the reactions were not completed at 800 °C. With increasing temperature the relative intensity of the peaks of intermediate phases progressively decreased and single phase compounds were obtained after heating at 1200 °C.

Fig. 2 shows the XRD patterns of the two series of LSCM-Ru compounds after treatment in air at 1400 °C. The X-ray diffractograms of the two series of compounds treated at 1400 °C showed only the peaks corresponding to the LSCM phase. The position of the diffraction peaks was independent of the Ru content up to x,y = 0.10. Increasing the fraction of Ru to x,y = 0.20 resulted in a shift of the peak position to lower 2θ and more convoluted peaks. The small changes of XRD pattern for x,y = 0.20 may indicate a change of symmetry of the perovskite structure [7]; however, neither additional peaks nor significant changes of the XRD patterns were detected. Therefore, both series of LSCM-Ru, with 0 ≤ x,y ≤ 0.20, were assumed to have the hexagonal structure of the parent compound LSCM. Recently, similar experimental findings were reported showing the complete substitution of Ni in LSCM up to 20 at.% [17].

More importantly, both Cr and Mn substitutions for Ru resulted in very weak lattice distortion as evidenced by the practically unchanged position of the diffraction peaks for x,y ≤ 0.10. To further investigate the structural properties of the LSCM-Ru series, the lattice parameters were calculated from the XRD data of Fig. 2. Fig. 3 shows the dependence of the lattice parameters a = b and c on the Ru fraction for both series of compounds (LSCxM-Ru and LSCMy-Ru). Calculated values were in perfect agreement with previously reported data for LSCM [7,23,24]. The calculated lattice parameters were practically independent on the Ru concentration up to x,y = 0.10 for both series. Such a feature is in agreement with the similar values of the ionic radius of six-coordinated Cr^{+3,+4}, Mn^{+3,+4}, and Ru^{+3,+4} [25]. However, Ru has a slightly higher ionic radius that is consistent with the increased c parameter observed for the x,y = 0.20 compounds.

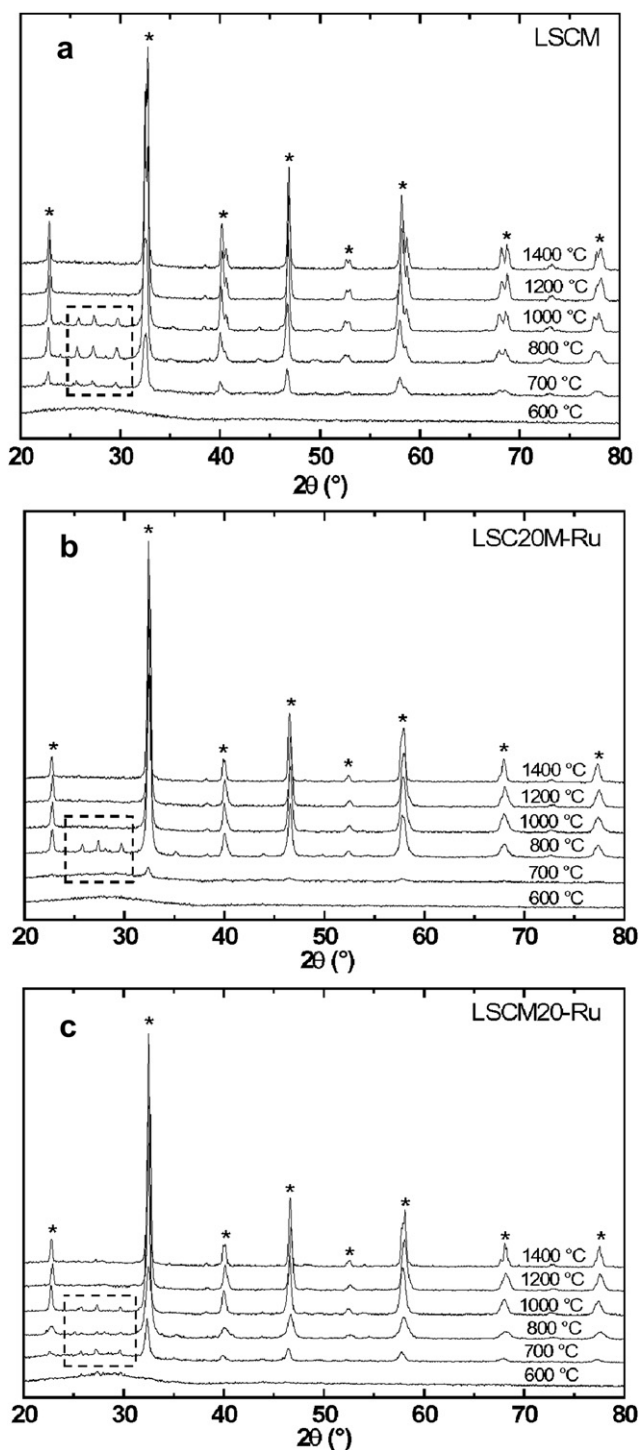


Fig. 1 – X-ray diffraction patterns of LSCM (a), LSC20M-Ru (b), and LSCM20-Ru (c) treated in air in the 600–1400 °C temperature range. The symbols (*) mark the indexed diffraction peaks of the compound LSCM [7] and the dotted rectangle encloses the 2θ range with peaks of intermediate phases.

Fig. 4 shows SEM micrographs of LSC10M-Ru (Fig. 4a and b) and LSCM10-Ru (Fig. 4c and d) powders treated in air at 1400 °C. The LSCM-Ru powders exhibited homogeneous distribution of particle sizes, with faceted grains with

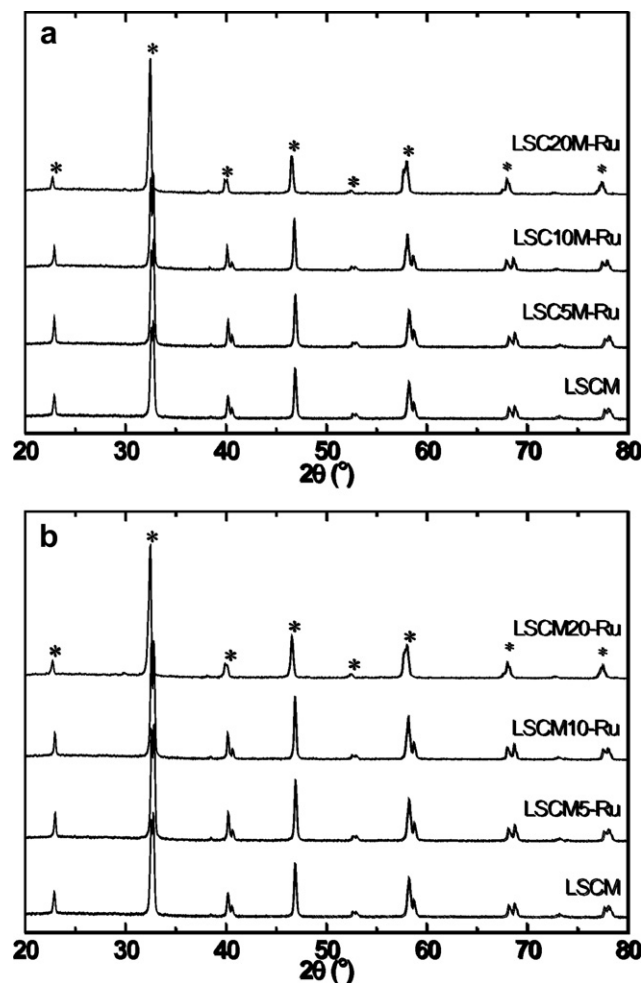


Fig. 2 – X-ray diffraction patterns of the series (a) LSC_xM-Ru and (b) LSCM_y-Ru after treatment in air at 1400 °C. The symbols (*) mark the indexed peaks of the compound LSCM [7].

estimated average size $\sim 1 \mu\text{m}$. In addition, no significant changes on the morphology of particles were observed in SEM analyses for both series, regardless the Ru content and the substituted ion (Cr or Mn).

The combined XRD and SEM results revealed that Ru substituted either Cr or Mn in the LSCM structure without causing significant lattice distortion or microstructural changes. It has been reported that the catalytic properties of similar Ru-substituted perovskites $\text{La}_{0.8}\text{Sr}_{0.2}\text{Cr}_{1-x}\text{Ru}_x\text{O}_{3-\delta}$ were significantly improved due to the segregation of Ru from the crystal structure [18]. More recently, it was reported that LSCM-Ni compounds exhibited a comparable effect, i.e., the segregation of Ni from the LSCM structure upon reduction, which resulted in Ni nanoparticles that were detected over the surface of larger particles of the parent compound [17].

In order to investigate both the stability of LSCM-Ru under reducing conditions and the possible segregation of Ru from the LSCM-Ru, treatments at 800 °C for 4 h under H_2 flow were carried out. The resulting powder samples were analyzed by XRD and TEM. Fig. 5 shows the XRD patterns of some selected reduced compositions of LSCM-Ru and the one of the as-prepared LSCM for comparison. The reducing treatment did

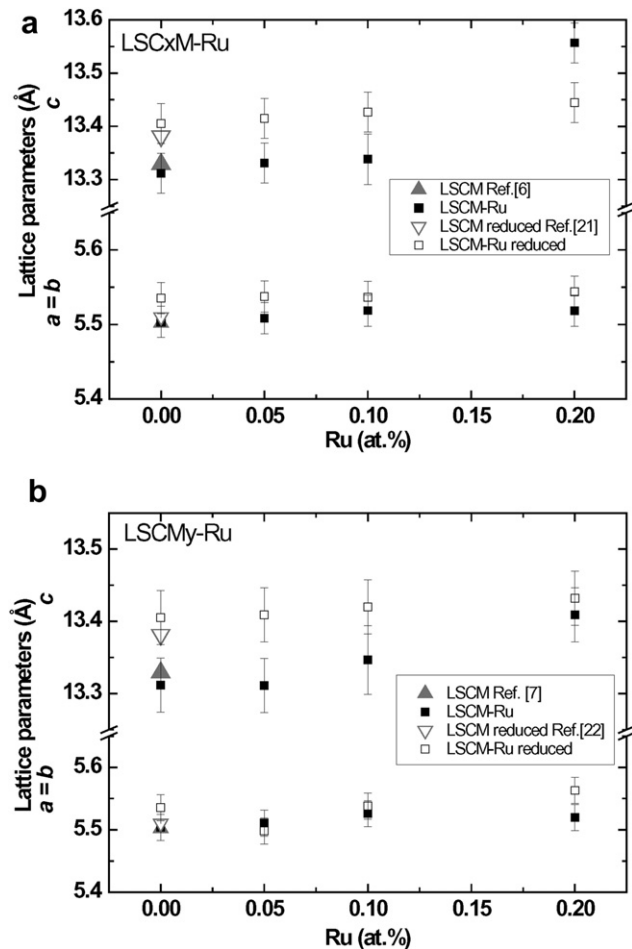


Fig. 3 – Lattice parameters dependence on the Ru content for the as-prepared and reduced samples of (a) LSCxM-Ru and (b) LSCMy-Ru. Values corresponding to previous reported data for both as-prepared [7] and reduced [24] samples are also shown.

not affect significantly the diffraction patterns, and neither phase transition nor additional peaks suggesting possible phase decomposition were found. The calculated lattice parameters of reduced LSCM-Ru samples were found to be close to the ones of as-prepared samples (Fig. 3), in agreement with previous results [7,17]. A slight increase of the *c* lattice parameter was probably related to both the loss of oxygen stoichiometry and Mn ion reduction [17]. Similarly to the as-prepared LSCM-Ru samples, lattice parameters of reduced samples were practically independent on the Ru content, as shown in Fig. 3.

The effects of the reducing treatment on LSCM-Ru specimens were further analyzed by TEM. Fig. 6 shows TEM images for the LSC20M-Ru compound. The TEM images of the reduced specimen (Fig. 6b) revealed spherical crystalline particles with size ~ 5 nm on the surface of larger particles, similarly to previous studies [17,18,20]. These spherical particles were absent in the as-prepared LSC20M-Ru sample (Fig. 6a). The images of the segregated rounded nanoparticles clearly showed the crystal planes indicating single crystalline particles (Fig. 6b). Such features allowed us to perform fast Fourier

transform analysis on the spherical particles to estimate the interplanar distance. Typical distances, as for example the plane indicated in the Fig. 6, were found to be $d = 0.232$ nm, in excellent agreement with $d = 0.234$ nm corresponding to the [0,0,1] plane of the hexagonal structure of Ru (ICSD n. 43710). The Ru segregation was also observed, although to a less extent, in samples with lower Ru content. The experimental results strongly suggested that similar effect takes place during the operation of the fuel cell using LSCM-Ru anodes. The presence of isolated Ru particles were associated with an enhanced performance of anodes and were pointed out to have interesting properties, such as a homogeneous distribution and limited coalescence at high temperatures, preserving the high surface area necessary for good catalytic activity [18].

Temperature programmed reduction (TPR) experiments were carried out in order to follow the transformations taking place during the reduction treatment of LSCM-Ru compounds. The reduction profiles of LSCM, LSC5M-Ru, and LSC20M-Ru samples are shown in Fig. 7. The TPR of LSCM exhibited no H_2 consumption up to $400^\circ C$, confirming the redox stability of LSCM. On the other hand, the samples with Ru addition (LSC5M-Ru and LSC20M-Ru) showed a peak at $T \sim 350^\circ C$ that is possibly related to the segregation of Ru. A possible mechanism is that Ru segregates as RuO_2 and is then reduced at $\sim 350^\circ C$. This result is in agreement with TEM analyses (Fig. 6), revealing that the reduction treatment promoted the formation of metallic Ru particles. Above $400^\circ C$, all samples exhibited a slight increase in H_2 consumption with increasing temperature that was probably related to the partial reduction of $Mn^{+3,+4}$.

3.2. Transport properties and fuel cell tests

The transport properties of LSCM-Ru compounds are of relevance and were investigated in a wide range of temperature, in both oxidizing and reducing atmosphere. The Arrhenius plots of the electrical conductivity (σ) are shown in Fig. 8. In static air (Fig. 8a), the LSCM-Ru compounds exhibited thermally activated behavior and σ values close to previously reported data [26,27]. The electrical transport properties of LSCM compounds were interpreted in terms of hopping of small polarons, and have been described by two thermally activated processes due to a small deviation from linearity at $T > 300^\circ C$ [1,26,28]. Such a smooth activation energy change was associated with a possible phase transition and suggests that no first-order transition occurred [1,7]. The LSCM-Ru $\sigma(T)$ showed in Fig. 8a shows a deviation from the linear behavior for $T > 300^\circ C$ and the experimental data were fitted to Arrhenius-type mechanism in both temperature ranges. The calculated E_a of LSCM sample were $E_a (T < 300^\circ C) = 190$ meV and $E_a (T > 300^\circ C) = 275$ meV, in perfect agreement with previously obtained values [1]. As observed in Fig. 8a, the addition of Ru did not affect significantly the transport mechanism of the LSCM and rather small changes of E_a were determined. For Cr substituted samples a slight decrease of E_a was observed, whereas for Mn substituted for Ru E_a values increased. The calculated E_a of samples with $x,y = 0.10$ were: LSC10M-Ru $E_a (T < 300^\circ C) = 189$ meV and $E_a (T > 300^\circ C) = 267$ meV; and LSCM10-Ru $E_a (T < 300^\circ C) = 195$ meV and $E_a (T > 300^\circ C) = 295$ meV. Although the transport mechanism remained practically unchanged

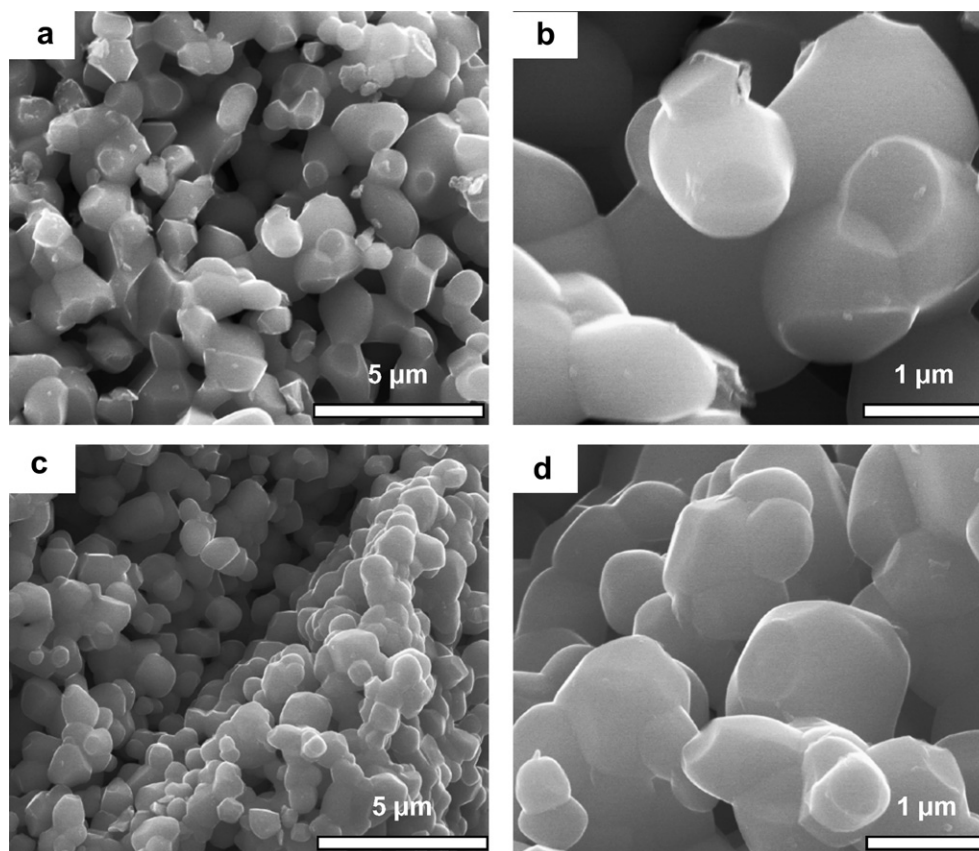


Fig. 4 – Scanning electron micrographs of LSC10M-Ru (a,b) and LSCM10-Ru (c,d) powders treated in air at 1400 °C.

upon Ru doping, the differences in $\sigma(T)$ magnitude were more pronounced than the ones of Ea [1,26]. The observed trends of both Ea and σ values can be correlated with the partial substitution of Mn and Cr for Ru in LSCM compounds.

The parent compound LSCM showed intermediate values of σ in comparison to the Ru substituted compounds. As a general trend, when Ru substituted Cr^{3+} there was an increase of σ , whereas the opposite was observed for $\text{Mn}^{3+,4+}$ substitutions. Deviations of such behavior, as for the $x = 0.05$ compound, are attributed to microstructural effects. The highest values of σ were observed for the LSC10M-Ru. Samples with high concentrations of Ru ($x \geq 10$) substituting Cr exhibited higher values of σ in relation to the remaining LSCM-Ru compounds. On the other hand, σ values were approximately one order of magnitude smaller when Ru substituted Mn. It was previously determined for the LSCM that Cr^{3+} is the predominant valence state of Cr in LSCM, suggesting that the hopping of charge carriers occurs primarily via the $\text{Mn}^{3+}-\text{O}_2-\text{Mn}^{4+}$ bonds [17,24,26]. Therefore, the observed features are in accordance with the $\sigma(T)$ dependence on the substituted cation. Such a dependence is also consistent with the transport properties of $(\text{La,Sr})(\text{Mn}_{1-z}\text{Cr}_z)\text{O}_3$, which showed an increased σ with decreasing z [2,17], adding further evidence for the selective substitution of both Cr^{3+} and $\text{Mn}^{3+,4+}$ for Ru in the LSCM.

In reducing atmosphere (Fig. 8b) an appreciable decrease of σ was observed, in agreement with the p-type conductivity of LSCM. However, samples with high concentration of Ru

($x,y \geq 10$) exhibited a less pronounced decrease of σ when atmosphere was switched to 4% H_2 . The conductivity of LSCM was previously found to progressively decrease for oxygen partial pressure $p\text{O}_2 < 10^{-13}$ atm [7,27]. It has been reported for LSCM that Cr remains in oxidation state 3+ even in reducing atmosphere, while Mn^{4+} is reduced to Mn^{3+} and charge compensation is achieved by oxygen vacancy formation [17,24]. Therefore, in reducing atmosphere the decrease of the $\sigma(T)$ of LSCM was concomitant with an increase in the Ea to 455 meV, which was related to an increased ionic transport [17,24]. Nevertheless, for samples with $x,y \geq 10$, the calculated Ea in reducing atmosphere were lower than the ones calculated for samples with low Ru content. However, similarly to the Ea in air, samples with Ru substituting Cr resulted in lower Ea than the ones with Mn substituted for Ru. For example, calculated Ea for samples LSC20M-Ru and LSCM20-Ru were 185 meV and 320 meV, respectively. Such feature indicated that Ru substitution, mainly in the Cr site, changed the charge compensation mechanism of the LSCM compound and favored the electronic transport in reducing atmosphere probably by promoting an increased mixed valence state of the B site of the perovskite. However, due to the multiple possible valence states of Ru it was difficult to infer the exact defect chemistry of LSCM-Ru compounds in reducing conditions. In order to determine the exact mechanism of charge transport further analysis, such as X-ray photoelectron spectroscopy, are required, but are beyond the scope of the present study.

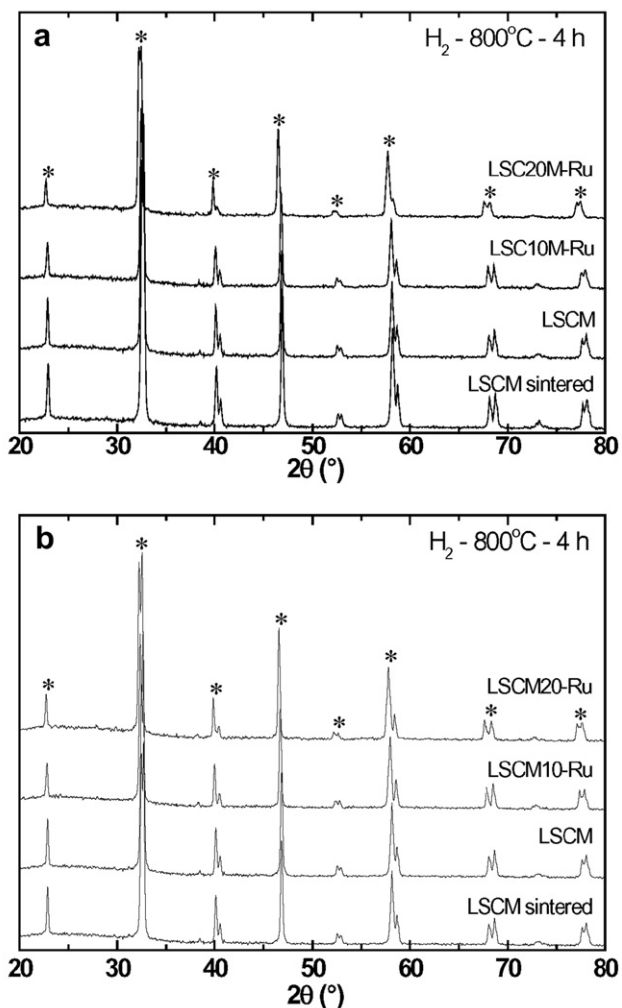


Fig. 5 – X-ray diffraction pattern of samples (a) LSC x M-Ru and (b) LSCM y -Ru with $x, y = 0, 10$, and 20 reduced under H_2 . For comparison, data for the as-prepared (sintered at $1400\text{ }^\circ\text{C}$) LSCM was included.

Based on the $\sigma(T)$ data in both air and reducing atmosphere, LSC x M-Ru compounds were chosen to be tested as anodes on single fuel cells. Initial tests revealed that fuel cells using an interfacial Ni/YSZ layer between the electrolyte and LSCM-Ru anode exhibited enhanced performance when compared to the ones with a single layer anode of LSCM-Ru [5]. Thus, single cells with LSM cathode, YSZ electrolyte, a functional Ni/YSZ layer (thickness $\sim 7\text{ }\mu\text{m}$), and a LSCM-Ru layer (thickness $\sim 10\text{ }\mu\text{m}$) were tested in both H_2 and dry ethanol.

The Fig. 9 shows the polarization curves of fuel cells with ceramic anode LSCM (Fig. 9a), LSC10M-Ru (Fig. 9b), and LSC20M-Ru (Fig. 9c) for H_2 and dry ethanol. Single cells exhibited OCV $\sim 1\text{ V}$ close to the Nernst value under humidified H_2 , but upon fuel change to ethanol the OCV dropped to $\sim 0.95\text{ V}$. Such a lower OCV value under ethanol may be due to the occurrence of partial oxidation [29] and/or steam reforming of ethanol reactions [30]. Since the fuel cells were initially tested under H_2 some steam was present as a result of draining current from the cell. Therefore, when

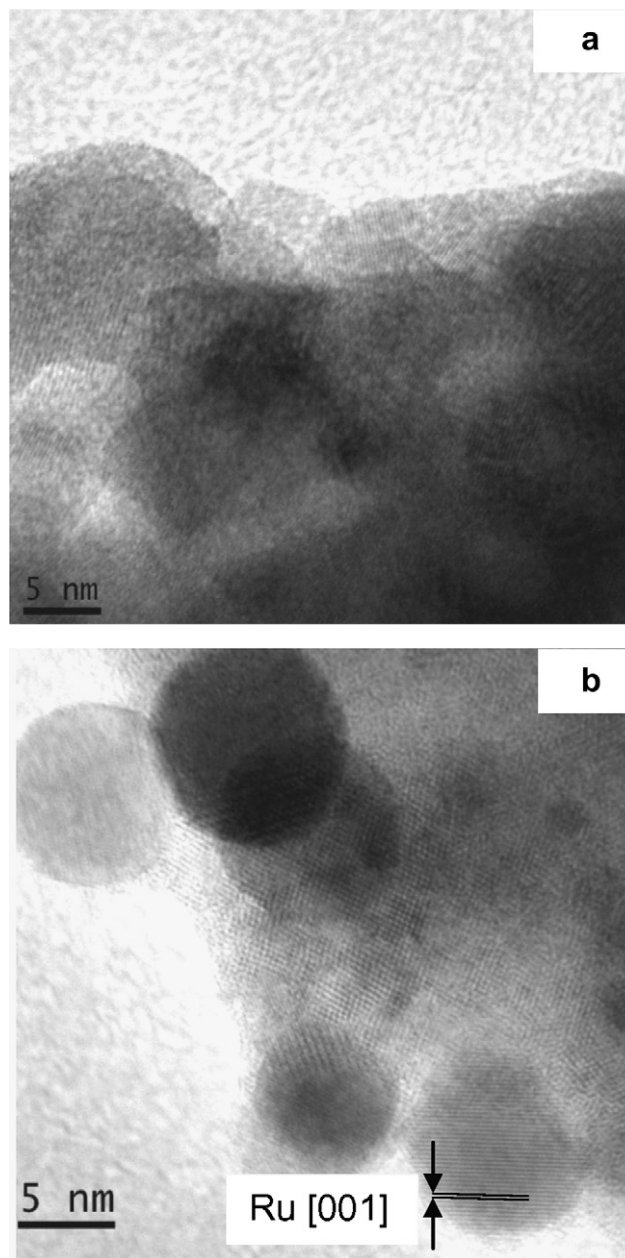


Fig. 6 – Transmission electron micrograph of the LSC20M-Ru (a) sintered at $1400\text{ }^\circ\text{C}$, before reduction; (b) reduced in H_2 .

fuel was switched to ethanol the remaining water molecules probably promoted the steam reforming reaction that sustained the fuel cell running in the so-called gradual internal reforming [31]. Recent results showed that steam reforming of ethanol in a SOFC resulted in OCV $\sim 0.97\text{ V}$ for $T > 760\text{ }^\circ\text{C}$ [15,32], in reasonable agreement with the measured values in the present study. Nevertheless, the most important observation from Fig. 9 was that the performance of single cells with LSCM-Ru anodes running on direct ethanol surpassed the one on H_2 [15]. In addition, the anodes with partial substitution of Cr by Ru ($x = 0.10$ and 0.20) exhibited higher performance than that of LSCM. The low current portions of the polarization curves were rather linear with low activation polarization, and the ohmic drop was the predominant

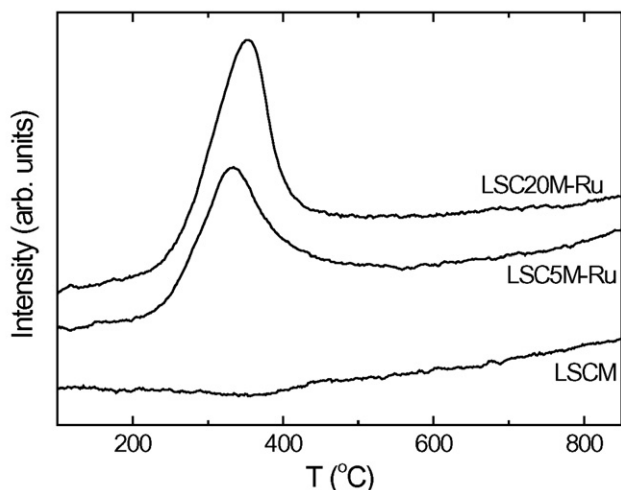


Fig. 7 – Temperature programmed reduction profiles of LSCM-Ru compounds.

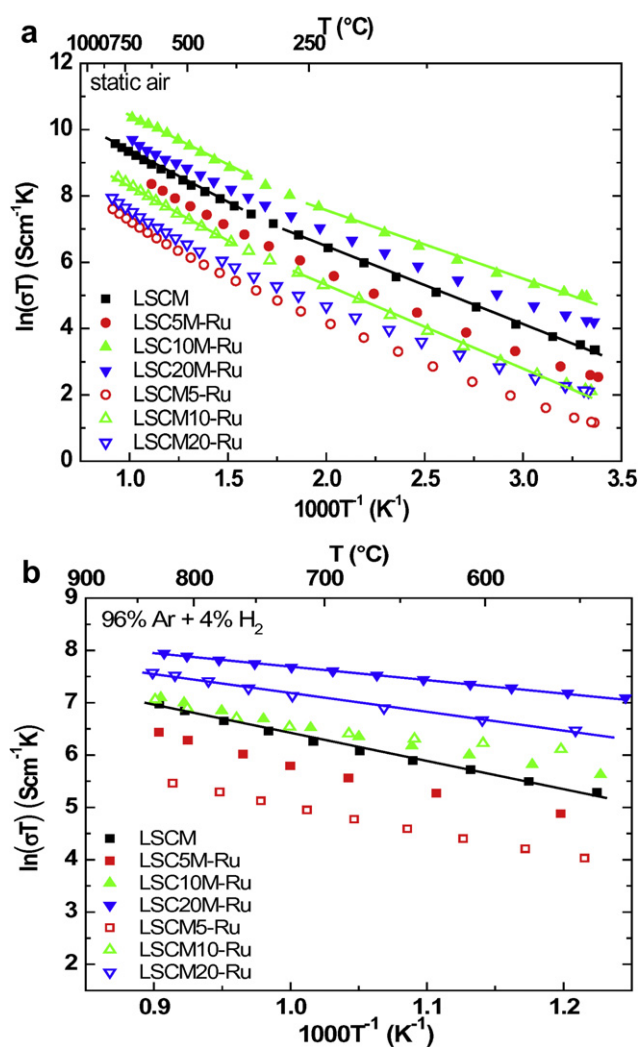


Fig. 8 – Arrhenius plot of LSCM-Ru compounds in air (a) and in 96% Ar + 4% H₂ (b). Straight lines correspond to the best linear fittings.

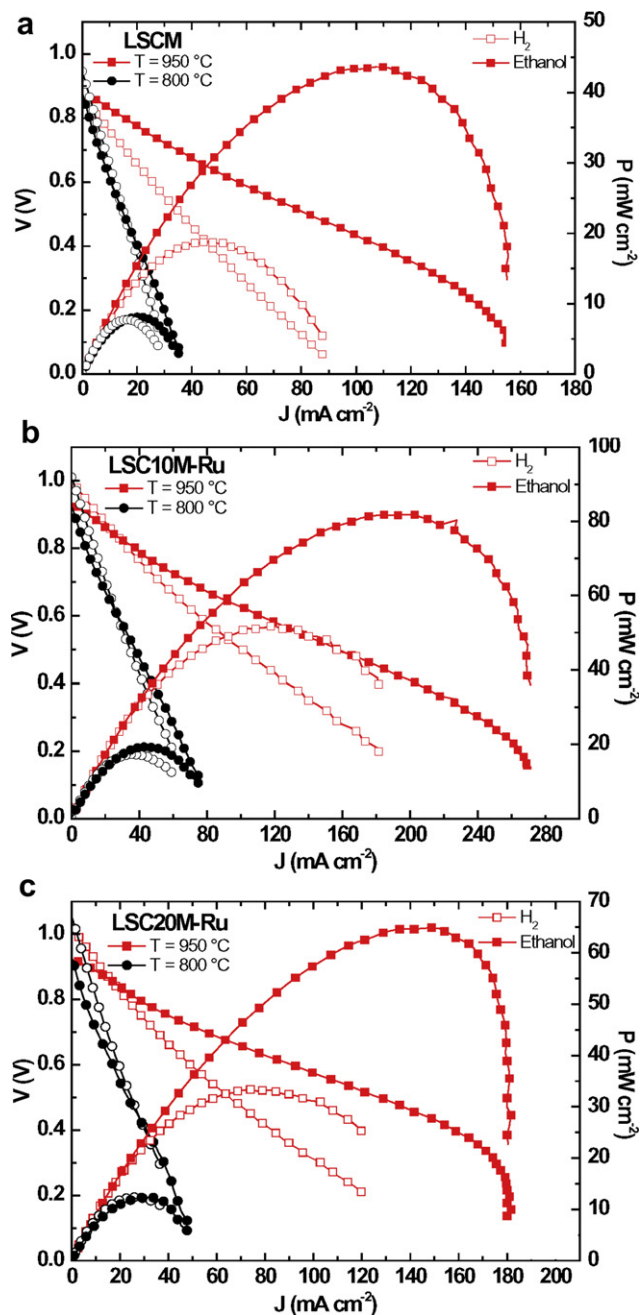


Fig. 9 – Polarization curves of single SOFCs with LSCM-Ru anodes running in H₂ and ethanol, measured at 800 °C and 950 °C (a) LSCM, (b) LSC10M-Ru, and (c) LSC20M-Ru.

polarization loss in both fuels. Such a feature was evidenced by increasing the measuring temperature to 950 °C, in which the conductivity of the LSCM-Ru increased considerably resulting in a significant enhancement of the fuel cell performance [15]. The enhanced performance of single cells running on ethanol is likely to be related to the transport properties of LSCxM-Ru anodes. As previously discussed, the p-type conductivity of the parent compound LSCM decreases progressively with decreasing oxygen partial pressure [7,24]. Therefore, it is expected that LSCM-Ru exhibits higher conductivity under ethanol than on H₂.

After operation, single cells were analyzed by SEM. The studied single cells showed comparable features and Fig. 10 shows a representative image of the cross section of the SOFC with LSCM10-Ru anode. In the SEM image the solid electrolyte (bottom) and the two anode layers can be discerned: the Ni/YSZ layer with $\sim 7 \mu\text{m}$ thick and the LSCM10-Ru layer with $\sim 10 \mu\text{m}$. The anode layers were found to have good adhesion to each other and an adequate microstructure displaying open pores and average grain sizes $\leq 1 \mu\text{m}$. More importantly, no apparent carbon formation was detected.

In order to further understand the effect of Ru addition on the LSCM-Ru anodes running on direct ethanol, impedance spectroscopy measurements were carried out at OCV during fuel cell testing. Fig. 11 shows the impedance diagrams of tested fuel cells at 950°C under both fuels.

The impedance data demonstrated that both the ohmic and the polarization resistances of the fuel cells decreased when the fuel was switched from H_2 to ethanol, adding further evidence that the observed enhancement of single SOFCs performance operating in ethanol was because the improved transport properties of LSCxM-Ru. Such experimental findings are in perfect agreement with recent reported data for SOFC running on ethanol/steam mixture using LSCM-based anodes [15]. At 950°C in ethanol, both anodes LSCxM-Ru with $x = 0.10$ and 0.20 showed comparable ohmic ($\sim 1 \Omega \text{cm}^2$) and polarization ($\sim 2 \Omega \text{cm}^2$) resistances, as roughly estimated from impedance data in Fig. 11b and c. Nonetheless, Ru-doped LSCM anodes had polarization resistances significantly lower than the ones for LSCM, indicating that the addition of Ru significantly enhanced the electrical properties of LSCM, in accordance with $\sigma(T)$ data shown in Fig. 8. In addition, the decreased polarization resistance observed for LSCxM-Ru anodes indicated that Ru played an important role for the catalytic activity for ethanol decomposition of LSCM compound.

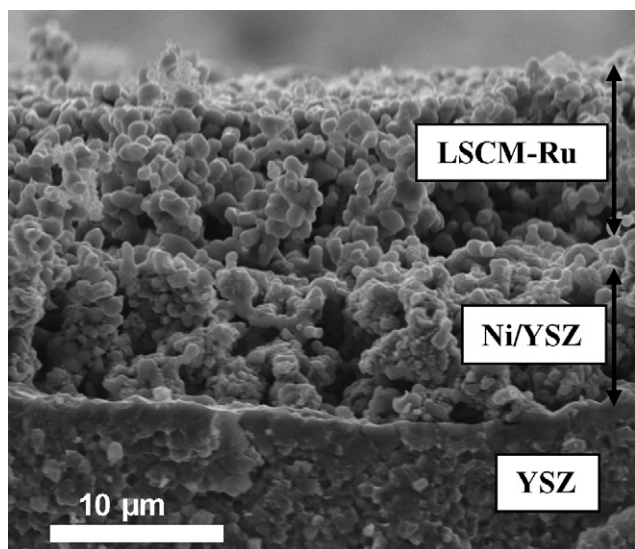


Fig. 10 – Cross section image of the anode after fuel cell operation. The Ni/YSZ and the LSCM10-Ru layers are identified.

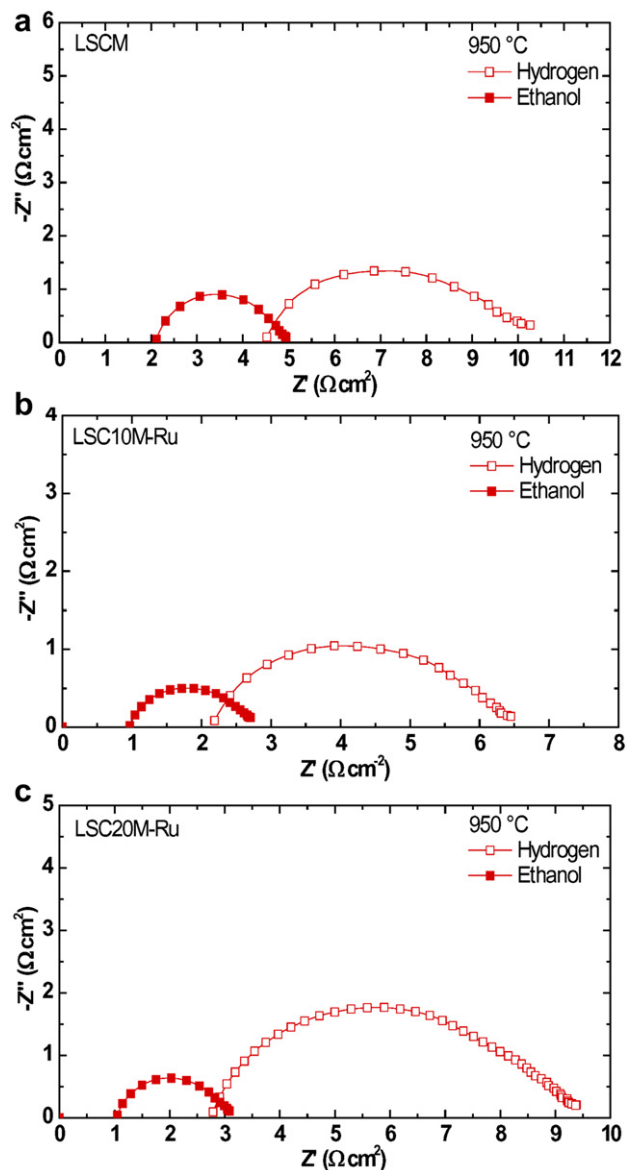


Fig. 11 – Impedance diagrams of single SOFCs with LSCM-Ru anodes measured at 950°C in both in H_2 and dry ethanol. (a) LSCM, (b) LSC10M-Ru, and (c) LSC20M-Ru.

Thus, in order to further investigate the catalytic properties of LSCM-Ru, these materials were tested for ED, SR, and POX of ethanol.

3.3. Catalytic properties of LSCM-Ru

Fig. 12 shows the ethanol conversion and product distributions as a function of time on stream (TOS) for ED over LSCM-Ru samples at 800°C . For all catalysts, ethanol conversion was complete and remained constant during 6 h of TOS. H_2 , CO and CH_4 were the main products formed along with a small amount of ethylene. These results indicate that ethanol decomposition to H_2 , CO and CH_4 and ethanol dehydration to ethylene were the only reactions taking place under these conditions. Ethylene is not predicted to be present at the thermodynamic equilibrium composition [33], suggesting that

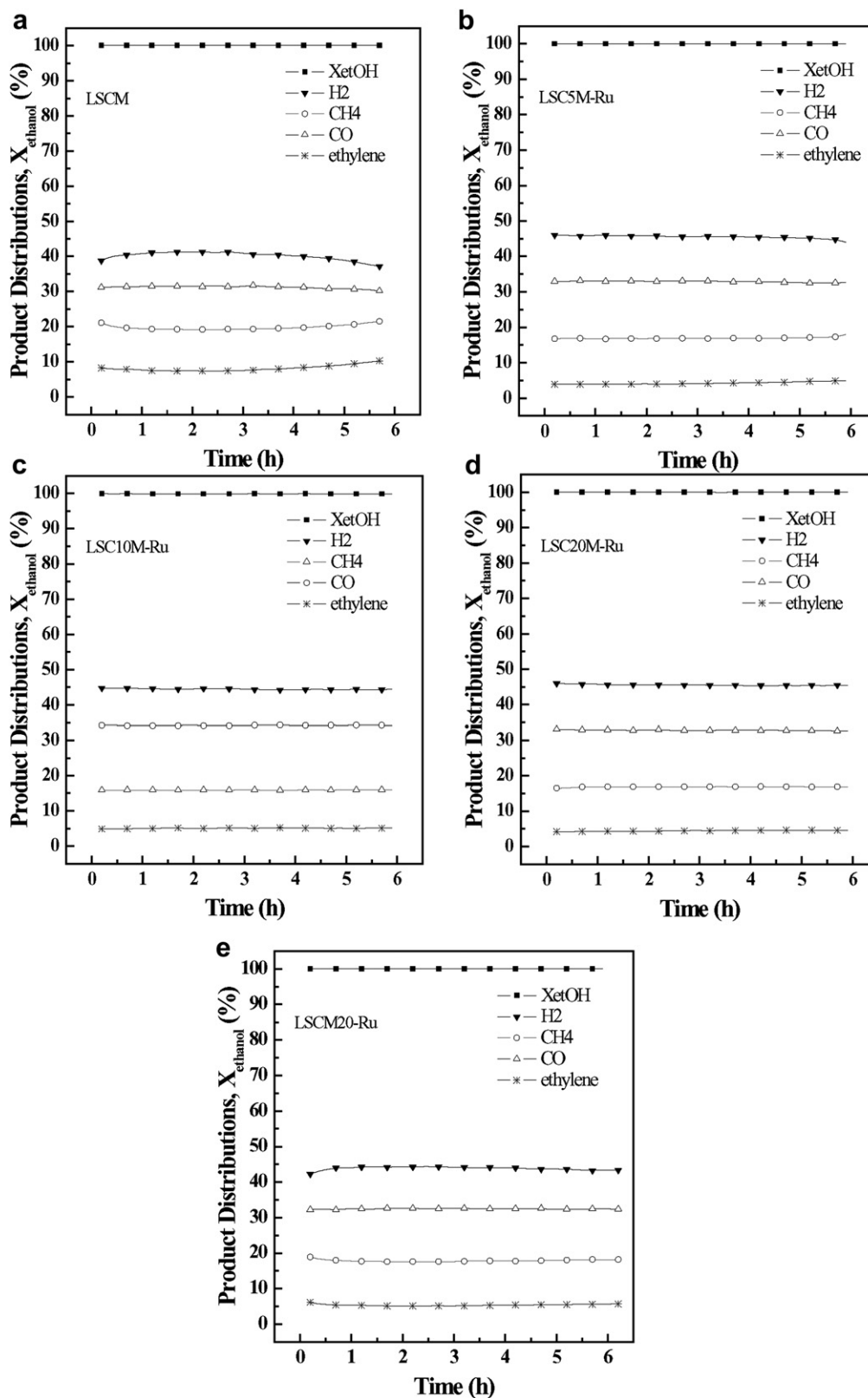


Fig. 12 – Ethanol conversion and product distributions as a function of time on stream (TOS) for ED over LSCM-Ru samples at 800 °C (a) LSCM, (b) LSC5M-Ru, (c) LSC10M-Ru, (d) LSC20M-Ru and (e) LSCM20-Ru.

under these conditions ethanol conversion reactions are kinetically controlled. The absence of CO_2 in the product distribution ruled out the occurrence of the ethanol reforming reaction, in agreement with the absence of water in the feed

[34]. For LSCM catalyst, the selectivity to H_2 decreased and the formation of ethylene increased with TOS. The substitution of Cr or Mn for Ru slightly improved the formation of H_2 and decreased the selectivity to ethylene. In addition, the

selectivity for all products remained rather constant when Ru was added to the catalysts, indicating that Ru improved the stability of the LSCM catalysts.

After ED reaction, the catalysts were carefully analyzed by SEM in order to evaluate possible carbon deposition. SEM images (Fig. 13) show the presence of some carbon filaments restricted to isolated areas mainly on the LSCM (Fig. 13a) and, in a less extent, on both the LSC5M-Ru and LSC10M-Ru (Fig. 13b and c, respectively). For LSC20M-Ru and LSCM20-Ru catalysts (Fig. 13d and e, respectively), SEM images revealed no carbon filaments, suggesting that the addition of higher Ru content inhibited the formation of carbon deposits during ED. The SEM findings were further confirmed by thermogravimetric analyses (not shown), which revealed that carbon

deposits correspond to ~ 1 wt.% for LSCM, whereas the addition of Ru in LSCM, as in $x,y > 0.10$ compounds, inhibited carbon formation.

In order to study the effect of water and oxygen in the feed on the carbon formation, the LSC5M-Ru material was tested on the SR and POX conditions. For such conditions, a low Ru content sample was chosen to be assumed the most susceptible composition for carbon formation. The ethanol conversion and product distributions as a function of TOS for SR and POX of ethanol over LSC5M-Ru catalyst are shown in Fig. 14. The addition of water to the feed significantly increased the selectivity toward hydrogen. Furthermore, the selectivity to CO and CH₄ decreased, as well as CO₂ formation was observed, but ethylene was no longer detected. These results indicated

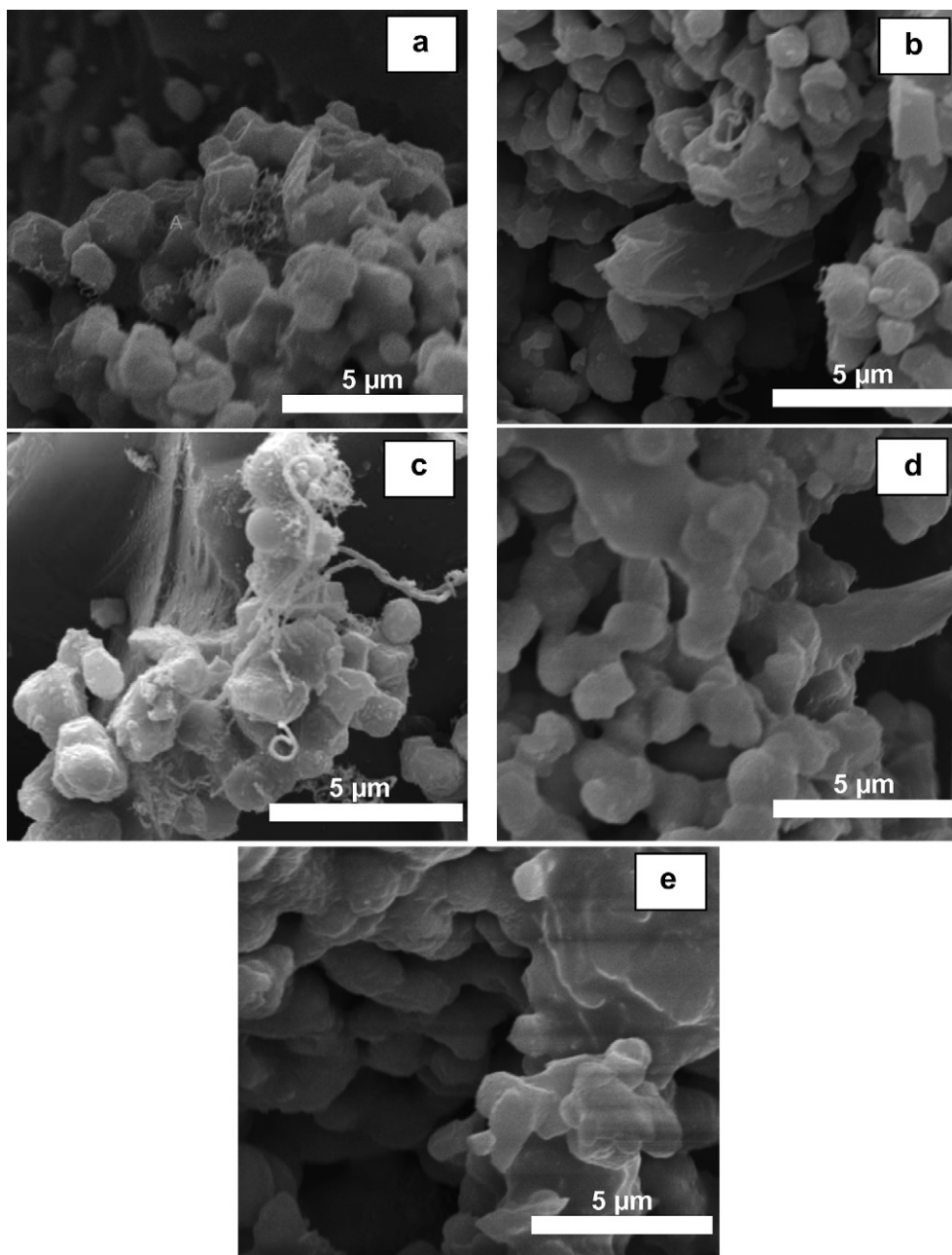


Fig. 13 – SEM images after ED of ethanol over (a) LSCM, (b) LSC5M-Ru, (c) LSC10M-Ru, (d) LSC20M-Ru and (e) LSCM20-Ru.

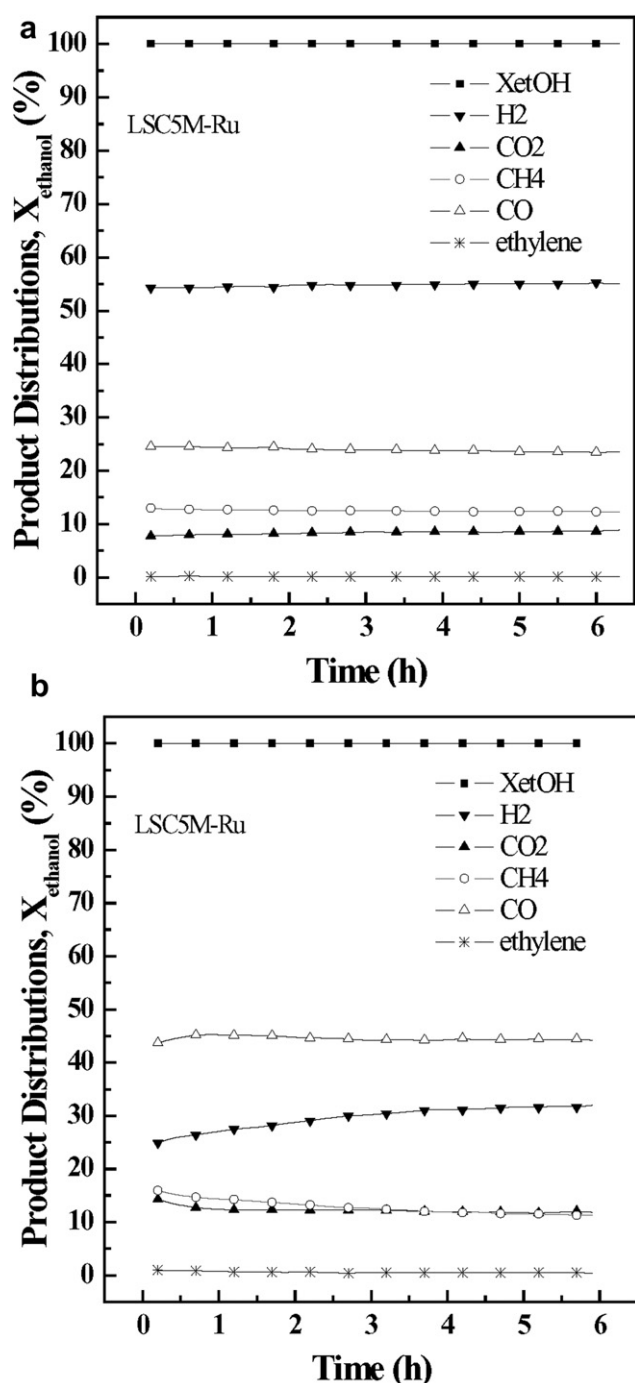


Fig. 14 – Ethanol conversion and product distributions as a function of time on stream (TOS) over LSC5M-Ru catalyst for (a) SR; (b) POX of ethanol at 800 °C.

that in the presence of water the steam reforming of ethanol to H₂ and CO₂ was the main reaction taking place instead of ethanol decomposition to CO and CH₄. Such a result adds further evidence to the gradual internal reforming of ethanol during fuel cell tests, as previously discussed [31]. In addition, since the SR is the catalytic test in which fuel cell operating conditions are closer resembled, the results suggested the good short-term stability of the LSCM-Ru anodes.

In the presence of oxygen, the selectivity to H₂ and CH₄ decreased whereas the formation of CO increased. Furthermore, CO₂ was also observed indicating that ethanol was oxidized. Ethylene was no longer detected in the presence of oxygen in the feed. SEM images of the LSC5M-Ru catalyst after SR and POX reactions did not show the presence of carbon filaments (Fig. 15). However, the SEM images revealed different microstructure of powders tested in SR and POX conditions. Although the average particle size remains similar, particles that were studied for SR reaction (Fig. 15a) showed a smoother surface than the ones for POX (Fig. 15b). Such feature is probably related to the different oxygen partial pressure during POX and SR reactions; however, a more detailed analysis is necessary to clear this point.

Recent studies using a thin LSCM-ceria composite layer deposited over Ni/ScSZ cermet and LSCM-ceria anodes tested in SOFC running on ethanol/steam mixtures revealed small amounts of carbon filaments in LSCM [5,15]. Such a carbon formation in LSCM anodes was attributed to a gas-phase

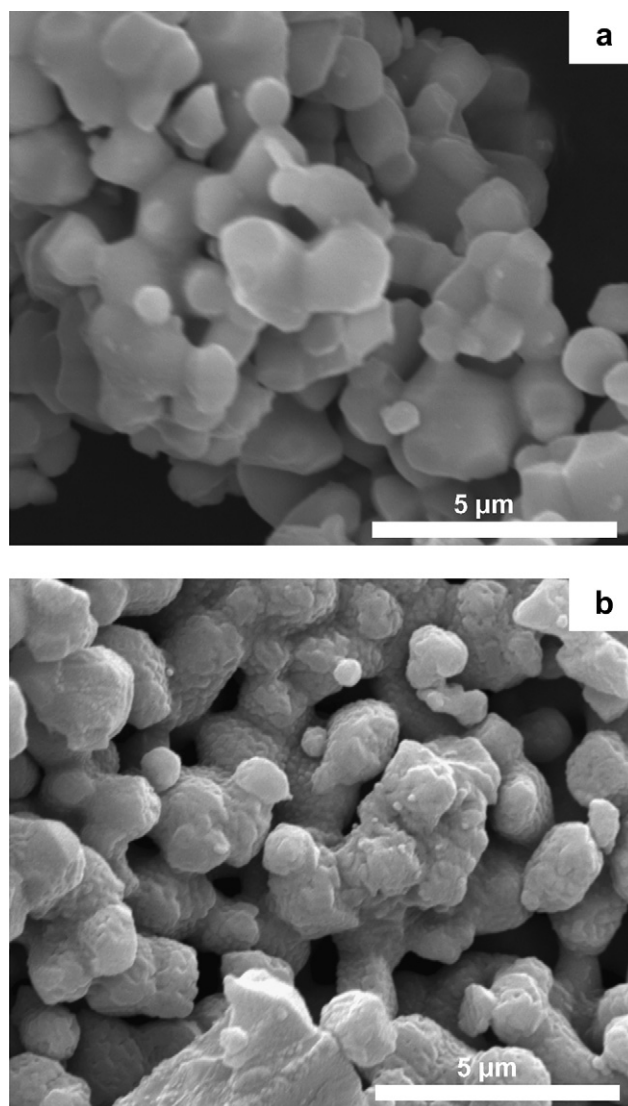


Fig. 15 – SEM images of LSC5M-Ru catalyst after (a) SR; (b) POX of ethanol at 800 °C.

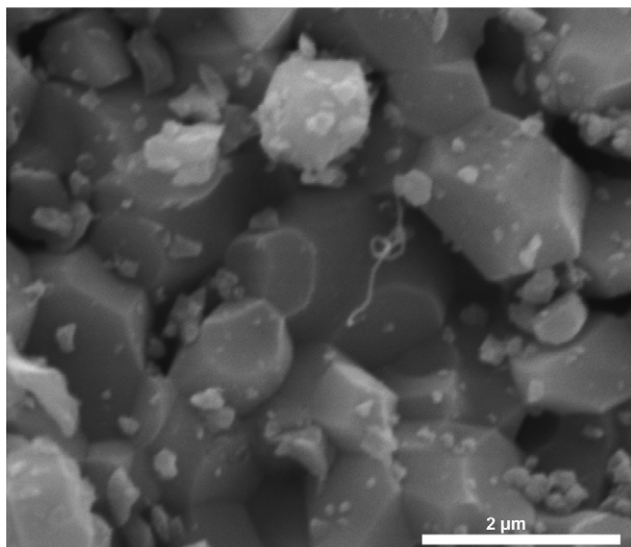


Fig. 16 – SEM images of LSCM perovskite after carburization with a mixture containing CH₄ (20%) in H₂ at 800 °C for 6 h.

deposition of carbon [15]; however, the exact mechanism of carbon formation was not further detailed.

According to the mechanism proposed for ethanol conversion reactions [34,35], ethanol adsorbs dissociatively over the metal oxide cation as an ethoxy species, followed by dehydrogenation to acetaldehyde and acetyl species. The dehydrogenated species may oxidize to acetate species, via the addition of support-bound hydroxyl groups. Then, the dehydrogenated and acetate species may decompose, producing CO and CH_x species, which may be further dehydrogenated to H and C. In the case of Ni, Co or Fe-based catalysts, this carbon can undergo: (i) reaction with water or oxygen; (ii) encapsulation of the metallic particle surface; or (3) dissolution into the metal crystallite followed by the nucleation and growth of carbon filaments.

Ni, Co, and Fe are the most intensively investigated metals used for hydrocarbon decomposition for the production of carbon nanotubes [36–38]. Elements with no carbon solubility in the metal or with multiple carbide phases were not able to produce carbon nanotubes [39]. For example, Cr, Mn, and La have sufficient carbon solubility in the solid solution. However, various intermediate carbides are formed instead of the graphite precipitation, inhibiting the formation of carbon nanotubes. However, it was observed that such elements could produce carbon nanotubes when carbide phases are previously formed or at elevated temperatures.

In fact, there are few works reporting the synthesis of carbon nanotubes with chromium-containing compounds [40,42]. The formation of carbon nanofibers and carbon nanocoils using Cr₂C₃ as catalyst has been described [41], and, more recently, the mechanism for carbon nanotube formation catalyzed by chromium carbide was investigated [42]. In order to study the mechanism of carbon growth based on chromium carbide, the carburization of the LSCM perovskite with a mixture containing CH₄ (20%) in H₂ at 800 °C for 6 h was carried out. SEM image (Fig. 16) of carburized LSCM catalyst

revealed the presence of carbon filaments. Therefore, the growth of carbon filaments on LSCM could be due to the formation of chromium carbide, similarly to the mechanism recently proposed [42]. On the other hand, in the presence of Ru nanoparticles, as in the LSCM-Ru compounds, the highly reactive carbon species might react with hydroxyl groups formed, preventing the accumulation of carbon.

4. Conclusions

Single phase La_{0.75}Sr_{0.25}Cr_{0.50}Mn_{0.50}O₃ (LSCM) compounds with partial substitution of Mn and Cr for Ru were synthesized by a polymeric precursor technique. A detailed characterization of the general properties of the fabricated materials revealed that Ru substitution favored the electronic transport in reduced oxygen partial pressure without significantly affecting the crystal structure of the parent compound LSCM. The combined effect of the addition of Ru on both the transport and catalytic properties to the LSCM anode resulted in increased performance of SOFC operating in dry ethanol. The experimental results indicate that partial substitution of a catalytic metal in the structure of perovskite anode is a promising strategy for direct ethanol solid oxide fuel cells.

Acknowledgments

This work was partially funded by CNPq, CAPES, FINEP, and CENEN. The authors thank CNPq for scholarships.

REFERENCES

- [1] Tao S, Irvine JTS. A redox-stable efficient anode for solid-oxide fuel cells. *Nat Mater* 2003;2:320–3.
- [2] Zheng Y, Ran R, Shao Z. Cr doping effect in B-site of La_{0.75}Sr_{0.25}MnO₃ on its phase stability and performance as an SOFC anode. *Rare Metals* 2009;28:361–6.
- [3] Lu XC, Zhu JH. Cu(Pd)-impregnated La_{0.75}Sr_{0.25}Cr_{0.5}Mn_{0.5}O_{3-δ} anodes for direct utilization of methane in SOFC. *Solid State Ionics* 2007;178:1467–75.
- [4] Jiang SP, Chen XJ, Chan SH, Kwok JT, Khor KA. GDC-impregnated (La_{0.75}Sr_{0.25})(Cr_{0.5}Mn_{0.5})O₃ anodes for direct utilization of methane in solid oxide fuel cells. *Solid State Ionics* 2005;177:149–57.
- [5] Zhu X, Lü Z, Wei B, Chen K, Liu M, Huang X, et al. Fabrication and performance of membrane solid oxide fuel cells with La_{0.75}Sr_{0.25}Cr_{0.5}Mn_{0.5}O_{3-δ} impregnated anodes. *J Power Sources* 2012;195:1793–8.
- [6] Muccillo R, Muccillo ENS, Fonseca FC, de Florio DZ. Characteristics and performance of electrolyte-supported solid oxide fuel cells under ethanol and hydrogen. *J Electrochem Soc* 2008;155:B232–5.
- [7] Tao S, Irvine JTS. Synthesis and characterization of (La_{0.75}Sr_{0.25})Cr_{0.5}Mn_{0.5}O_{3-δ}, a redox-stable, efficient perovskite anode for SOFCs. *J Electrochem Soc* 2004;151:A252–9.
- [8] Kim J, Nair VV, Vohs JM, Gorte RJ. A study of the methane tolerance of LSCM-YSZ composite anodes with Pt, Ni, Pd and ceria catalysts. *Scripta Mater* 2011;65:90–5.

- [9] Zhang L, Chen X, Jiang SP, He HQ, Xiang Y. Characterization of doped $\text{La}_{0.7}\text{A}_{0.3}\text{Cr}_{0.5}\text{Mn}_{0.5}\text{O}_{3-\delta}$ ($\text{A} = \text{Ca}, \text{Sr}, \text{Ba}$) electrodes for solid oxide fuel cells. *Solid State Ionics* 2009;180:1076–82.
- [10] Babaei A, Zhang L, Tan SL, Jiang SP. Pd-promoted (La, Ca)(Cr, Mn) O_3 /GDC anode for hydrogen and methane oxidation reactions of solid oxide fuel cells. *Solid State Ionics* 2010;181:1221–8.
- [11] Liu J, Madsen BD, Ji Z, Barnett SA. A fuel-flexible ceramic-based anode for solid oxide fuel cells. *Electrochem Solid-State Lett* 2002;5:A122–4.
- [12] Jiang SP, Chan SH. A review of anode materials development in solid oxide fuel cells. *J Mater Sci* 2004;39:4405–39.
- [13] Barison S, Fabrizio M, Mortalò C, Antonucci P, Modafferi V, Gerbasi R. Novel $\text{Ru}/\text{La}_{0.75}\text{Sr}_{0.25}\text{Cr}_{0.5}\text{Mn}_{0.5}\text{O}_{3-\delta}$ catalysts for propane reforming in IT-SOFCs. *Solid State Ionics* 2010;181:285–91.
- [14] Jiang SP, Ye Y, He T, Ho S. Nanostructured palladium- $\text{La}_{0.75}\text{Sr}_{0.25}\text{Cr}_{0.5}\text{Mn}_{0.5}\text{O}_3/\text{Y}_2\text{O}_3\text{-ZrO}_2$ composite anodes for direct methane and ethanol solid oxide fuel cells. *J Power Sources* 2008;185:179–82.
- [15] Corre GPG, Irvine JTS. Studies on direct ethanol use in SOFCs. *ECS Trans* 2011;35:2845–54.
- [16] Ye X, Wang SR, Wang ZR, Hu Q, Sun XF, Wen TL, et al. Use of $\text{La}_{0.75}\text{Sr}_{0.25}\text{Cr}_{0.5}\text{Mn}_{0.5}\text{O}_3$ materials in composite anodes for direct ethanol solid oxide fuel cells. *J Power Sources* 2008;183:512–7.
- [17] Jardiel T, Caldes MT, Moser F, Hamon F, Gauthier G, Joubert O. New SOFC electrode materials: the Ni-substituted LSCM-based compounds $(\text{La}_{0.75}\text{Sr}_{0.25})(\text{Cr}_{0.5}\text{Mn}_{0.5-x}\text{Ni}_x)\text{O}_{3-\delta}$ and $(\text{La}_{0.75}\text{Sr}_{0.25})(\text{Cr}_{0.5-x}\text{Ni}_x\text{Mn}_{0.5})\text{O}_{3-\delta}$. *Solid State Ionics* 2010;181:894–901.
- [18] Kobsiriphat W, Madsen BD, Wang Y, Marks LD, Barnett SA. $\text{La}_{0.8}\text{Sr}_{0.2}\text{Cr}_{1-x}\text{Ru}_x\text{O}_{3-\delta}\text{-Gd}_{0.1}\text{Ce}_{0.9}\text{O}_{1.95}$ solid oxide fuel cell anodes: Ru precipitation and electrochemical performance. *Solid State Ionics* 2009;180:257–64.
- [19] Sauvet AL, Irvine JTS. Catalytic activity for steam methane reforming and physical characterisation of $\text{La}_{1-x}\text{Sr}_x\text{Cr}_{1-y}\text{Ni}_y\text{O}_{3-\delta}$. *Solid State Ionics* 2004;167:1–8.
- [20] Kobsiriphat W, Madsen BD, Wang Y, Shah M, Marks LD, Barnett SA. Nickel- and ruthenium-doped lanthanum chromite anodes: effects of nanoscale metal precipitation on solid oxide fuel cell performance. *J Electrochem Soc* 2010;157:B279–84.
- [21] Fonseca FC, Muccillo R. Properties of $\text{YBa}_2\text{Cu}_3\text{O}_{7-\delta}\text{-Ag}$ superconductors prepared by the citrate method. *Physica C* 1996;267:87–92.
- [22] Monteiro NK, Nóbrega SD, Fonseca FC. Ceramic oxide anode with precipitated catalytic nanoparticles for ethanol fueled SOFC. *ECS Trans* 2011;35:1601–9.
- [23] Estemirova S, Fetisov A, Balakirev V, Titova S. Crystal structure and magnetic properties of $(\text{La}_{1-x}\text{Sr}_x\text{MnO}_3)\text{N}$ (LaCrO_3) $_{1-\text{N}}$ solid solutions. *J Supercond Novel Magn* 2006;20:113–6.
- [24] Lay E, Gauthier G, Dessemond L. Preliminary studies of the new ce-doped La/Sr chromo-manganite series as potential SOFC anode or SOEC cathode materials. *Solid State Ionics* 2011;189:91–9.
- [25] Shannon RD. Revised effective ionic radii and systematic studies of interatomic distances in halides and chalcogenides. *Acta Crystallogr* 1976;A32:751–67.
- [26] Fonseca FC, Muccillo ENS, Muccillo R, de Florio DZF. Synthesis and electrical characterization of the ceramic anode $\text{La}_{1-x}\text{Sr}_x\text{Mn}_{0.5}\text{Cr}_{0.5}\text{O}_3$. *J Electrochem Soc* 2008;155:B483–7.
- [27] Lay E, Gauthier G, Rosini S, Savaniu C, Irvine JTS. Ce-substituted LSCM as new anode material for SOFC operating in dry methane. *Solid State Ionics* 2008;179:1562–6.
- [28] Raffaele R, Anderson HU, Sparlin DM, Parris PE. Evidence for a crossover from multiple trapping to percolation in the high-temperature electrical conductivity of Mn-doped LaCrO_3 . *Phys Rev Lett* 1990;65:1383–6.
- [29] Park S, Vohs JM, Gorte RJ. Direct oxidation of hydrocarbons in a solid-oxide fuel cell. *Nature* 2000;404:265–7.
- [30] Leo TJ, Raso MA, Navarro E, Sánchez-de-la-Blanca E. Comparative exergy analysis of direct alcohol fuel cells using fuel mixtures. *J Power Sources* 2011;196:1178–83.
- [31] (a)Vernoux P, Guindet J, Kleitz M. Gradual internal methane reforming in intermediate-temperature solid-oxide fuel cells. *J Electrochem Soc* 1998;145:3487–92; (b)Georges S, Parrour G, Henault M, Fouletier J. Gradual internal reforming of methane: a demonstration. *Solid State Ionics* 2006;177:2109–12; (c)Klein JM, Hénault M, Roux C, Bultel Y, Georges S. Direct methane solid oxide fuel cell working by gradual internal steam reforming: analysis of operation. *J Power Sources* 2009;193:331–7.
- [32] Diethelm S, Van herle J. Ethanol internal steam reforming in intermediate temperature solid oxide fuel cell. *J Power Sources* 2011;196:7355–62.
- [33] (a)Garcia EY, Laborde MA. Hydrogen production by the steam reforming of ethanol: thermodynamic analysis. *Int J Hydrogen Energy* 1991;16:307–12; (b)Rabenstein G, Hacker VJ. Hydrogen for fuel cells from ethanol by steam-reforming, partial-oxidation and combined auto-thermal reforming: a thermodynamic analysis. *J Power Sources* 2008;185:1293–304.
- [34] de Lima SM, da Cruz IO, Jacobs G, Davis BH, Mattos LV, Noronha FB. Steam reforming, partial oxidation, and oxidative steam reforming of ethanol over Pt/CeZrO_2 catalyst. *J Catal* 2008;257:356–68.
- [35] (a)de Lima SM, da Cruz IO, Jacobs G, Davis BH, Mattos LV, Noronha FB. Study of catalyst deactivation and reaction mechanism of steam reforming, partial oxidation, and oxidative steam reforming of ethanol over Co/CeO_2 catalyst. *J Catal* 2009;268:268–81; (b)de Lima SM, da Silva AM, Graham UM, Jacobs G, Davis BH, Mattos LV, et al. Ethanol decomposition and steam reforming of ethanol over CeZrO_2 and Pt/CeZrO_2 catalyst: reaction mechanism and deactivation. *Appl Catal A General* 2009;352:95–113.
- [36] (a)Rostrup-Nielsen JR. Production of synthesis gas. *Catal Today* 1993;18:305–24; (b)Rostrup-Nielsen JR, Rostrup-Nielsen T. Large-scale hydrogen production. *Cattech* 2002;6:150–9.
- [37] Li Y, Li D, Wang G. Methane decomposition to CO_x -free hydrogen and nano-carbon material on group 8–10 base metal catalysts: a review. *Catal Today* 2011;162:1–48.
- [38] Muradov NZ, Veziroglu TN. From hydrocarbon to hydrogen-carbon to hydrogen economy. *Int J Hydrogen Energy* 2005;30:225–37.
- [39] Deck CP, Vecchio K. Prediction of carbon nanotube growth success by the analysis of carbon-catalyst binary phase diagrams. *Carbon* 2006;44:267–75.
- [40] (a)Okuyama F, Ogasawara I. Chromium-containing metallic fibers confined within carbon nanotubes: possibility of template-mediated crystal growth. *Appl Phys Lett* 1997;71:623–5; (b)Okuyama F, Hayashi T, Fujimoto Y. Graphite lattice synthesis catalyzed by chromium-containing crystallites. *Appl Phys Lett* 1993;74:3726–8.
- [41] Yang S, Chen X, Kikuchi N, Motojima S. Catalytic effects of various metal carbides and Ti compounds for the growth of carbon nanocoils. *Mater Lett* 2008;62:1462–5.
- [42] Li H, Cui X, Chen W. Mechanism of coke formation caused by catalytic nanochromium carbide particles from decomposition of CeCrO_3 . *J Am Ceram Soc* 2011;94:2578–84.